

## Research Article

# WO<sub>3</sub> Nanowires on Graphene Sheets as Negative Electrode for Supercapacitors

**Bo Liu, Yan Wang, Hong-Wu Jiang, and Ben-Xue Zou**

*Department of Chemical Engineering, Eastern Liaoning University, Dandong, China*

Correspondence should be addressed to Ben-Xue Zou; [benxue\\_dd@163.com](mailto:benxue_dd@163.com)

Received 12 December 2016; Accepted 16 January 2017; Published 20 February 2017

Academic Editor: Jianlin Li

Copyright © 2017 Bo Liu et al. This is an open access article distributed under the Creative Commons Attribution License, which permits unrestricted use, distribution, and reproduction in any medium, provided the original work is properly cited.

WO<sub>3</sub> nanowires directly grown on graphene sheets have been fabricated by using a seed-mediated hydrothermal method. The morphologies and electrochemical performance of WO<sub>3</sub> films prepared by different process were studied. The results show that the precoated nanoseeds and graphene sheets on graphite electrode provide more reactive centers for the nucleation and formation of uniform WO<sub>3</sub> nanowires. The WO<sub>3</sub> nanowires electrode exhibits a high area specific capacitance of 800 mF cm<sup>-2</sup> over negative potential range from -1.0 V to 0 V versus SCE in 1 M Li<sub>2</sub>SO<sub>4</sub> solution. A high performance electrochemical supercapacitor assembled with WO<sub>3</sub> nanowires as negative electrode and PANI/MnO<sub>2</sub> as positive electrodes over voltage range of 1.6 V displays a high volumetric capacitance of 2.5 F cm<sup>-3</sup>, which indicate great potential applications of WO<sub>3</sub> nanowires on graphene sheets as negative electrode for energy storage devices.

## 1. Introduction

Nanostructured tungsten oxide materials have received increasing attention due to their great potential applications in gas sensors, photocatalysts, field-emission devices, and electrochromic and energy storage devices [1–6]. Nanostructured tungsten oxides as electrode materials are expected to display enhanced electrochemical performance because of their large surface area and low charge transport resistance. Among the various nanostructures, one-dimensional (1D) structures such as nanowires and nanotubes are especially attractive for dimensionality and size which have been regarded as significant factors that may bring novel and excellent properties [7–14].

A wide variety of synthesis methods, including physical or chemical vapor deposition and wet-chemical process, have been used to produce 1D WO<sub>x</sub>. Shingaya and coworkers fabricated 1D WO<sub>x</sub> by heating of W or WO<sub>x</sub> powders at high temperature in the presence of oxygen to form WO<sub>x</sub> vapors that condense onto a colder substrate [15]. Rao and Zheng presented flame synthesis of tungsten oxide nanostructures on a variety of substrates using a coflow multielement diffusion burner [16]. The nanostructured WO<sub>x</sub> film can be directly grown on substrate by vapor deposition, but high

cost, high temperature, and various synthesis parameters to control limit the widespread of this method to large-scale applications. Wet-chemical process is regarded as a simple and low cost method to prepare WO<sub>x</sub> nanostructures. Polleux and coworkers represented template-free synthesis method to produce outstanding aspect ratio of WO<sub>3</sub> nanowires with tungsten isopropoxide and benzyl alcohol as raw materials [17]. The film assembled by drop-coating and followed by calcination at 500°C in air to remove organic compound exhibited high sensibility to low NO<sub>2</sub> concentrations. Wang et al. synthesized WO<sub>3</sub> nanorods by a facile hydrothermal process and constructed transparent film by drop-coating on ITO glass for electrochromic applications [18].

WO<sub>3</sub> is also considered to be an attractive electrode material for energy storage devices due to intercalation/deintercalation of electrons and protons or Li<sup>+</sup> into the oxide [19–22]. But low conductivity and poor rate performance of tungsten oxide limit its wide application for pseudocapacitors. One way to improve the performance of tungsten oxide is to combine WO<sub>3</sub> with other conductive materials such as conducting polymers, carbon fibers and reduced graphene oxide [23–25]. However, much work has been focused on WO<sub>3</sub> electrode as positive electrode, but little has been reported for WO<sub>3</sub> as negative electrode for

supercapacitors [26, 27]. Moreover, ordered nanostructures grown directly on the electrode substrate without the need for polymer binders is particularly important, because most polymer binders are electrochemically inactive for charge storage. In this work, we present a simple and convenient method to fabricate tungsten oxide nanowires directly grown on graphene sheets by simple seed-mediated hydrothermal method. Morphologies and microstructures of the samples were investigated by field-emission scanning electron microscopy (SEM) and transmission electron microscopy (TEM), while cyclic voltammetry (CV), chronopotentiometry (CP), and AC impedance were carried out to study capacitive properties of the films. A comparative analysis of different preparation process on the morphologies and performance of the films was studied.

## 2. Experimental Section

**2.1. Preparation of Tungsten Oxide Nanowires on Graphene Sheets.** The preparation of graphene sheets partially exfoliated from graphite foil was according to our previous work [28]. Graphite foil was purchased from SGL (Germany). Tungsten oxide nanowires on graphene sheets were synthesized by using a seed-mediated hydrothermal method. The partially exfoliated graphite foil (Ex-GF) was firstly dipped into  $\text{H}_2\text{WO}_4$  suspension (pH = 1), followed by annealing at  $250^\circ\text{C}$  on a hot-plate for 10 min. The  $\text{H}_2\text{WO}_4$  suspension was prepared by adding 0.6 g  $\text{Na}_2\text{WO}_4$ , 5 mL distilled water, and a certain amount of 3 M HCl to adjust pH value of 1. The dip-coating and drying processes were repeated for 3 times. The obtained seeded substrate was then transferred into a Teflon-lined stainless steel autoclave with hydrothermal reaction solution. The graphite foil was placed against the inner wall of the autoclave with the seeded face downward. The solution used for hydrothermal reaction contained 0.6 g sodium tungstate ( $\text{Na}_2\text{WO}_4$ ), 0.29 g NaCl, 15 mL distilled water, and an amount of HCl to adjust the pH value of the solution to 2.5. Then the autoclave was sealed and maintained at  $180^\circ\text{C}$  for 24 h in an oven. After hydrothermal reaction, the graphite foil was removed from the vessel and washed thoroughly with distilled water and then dried at  $50^\circ\text{C}$  for 6 h. The graphite foil was covered with a uniform film. The obtained sample was denoted as NW/Ex-GF (or NW).

To improve the stability of the sample, the as-synthesized film on graphite foil was then treated by charge/discharge process with a potential range of  $-1.0\sim 0\text{ V}$  in 1 M  $\text{Li}_2\text{SO}_4$  electrolyte at  $1\text{ mA cm}^{-2}$  for 5 cycles, followed by washing with distilled water and annealing at  $350^\circ\text{C}$  for 1 h in  $\text{N}_2$  atmosphere. The obtained sample after posttreatment is denoted as ANW/Ex-GF (or ANW). To study the influence of the preparation process on the morphologies and properties of the films, other three different  $\text{WO}_x$  films were prepared. The  $\text{WO}_x$  film prepared by hydrothermal process without precoating nanoseeds on graphene sheets was denoted as NW with no seeding. The  $\text{WO}_x$  film prepared without exfoliating graphite foil was denoted as NW with no graphene sheets, and the film prepared without adding NaCl in the deposition solution was denoted as NW with no NaCl, respectively. The

other condition was kept same as NW and those samples were not posttreated.

**2.2. Preparation of PANI/ $\text{MnO}_2$  for Positive Electrode.** Hybrid film of PANI/ $\text{MnO}_2$  was electrochemically deposited on graphene sheets partially exfoliated from graphite foil through 20 cyclic voltammetric scans from  $-0.2$  to  $1.0\text{ V}$  (versus SCE) at  $10\text{ mV s}^{-1}$  from solutions of 0.1 M aniline containing 160 mM  $\text{MnSO}_4$  and 1 M  $\text{H}_2\text{SO}_4$ . The obtained sample PANI/ $\text{MnO}_2$  on graphite foil is denoted as PM electrode.

**2.3. Fabrication of Asymmetric Supercapacitor Devices.** Asymmetric supercapacitors were assembled by using PM as the positive and ANW as the negative electrode and  $\text{Li}_2\text{SO}_4$ /PVA gel as the electrolyte as well as separator, similar to our previously reported supercapacitors assembled by gel electrolyte [29]. The working area of two electrodes was  $1.0 \times 1.0\text{ cm}^2$ .

**2.4. Characterization.** The morphologies of the samples were investigated by field-emission scanning electron microscopy (SEM, Carl Zeiss, Germany) and transmission electron microscopy (TEM, JEOL, Japan). X-ray diffraction (XRD) patterns were recorded on an X-ray diffractometer (PW3040/60, PANalytical B.V., Netherlands) employing monochromatized Cu  $\text{K}\alpha$  incident radiation. XPS spectra were recorded on Thermo ECSALAB 250 electron spectrometer using Al  $\text{K}\alpha$  radiation (1486.6 eV). Electrochemical experiments were conducted with a CHI660e potentiostat in a three-electrode electrolytic cell. The reference and counter electrodes were saturated calomel electrode (SCE) and platinum wire, respectively. Pseudocapacitive behaviors of the films were studied by cyclic voltammetry (CV) and chronopotentiometry (CP) in 1 M  $\text{Li}_2\text{SO}_4$  electrolyte. EIS spectra were measured on CHI660e potentiostat with electrochemical impedance software Power Sine. The potential amplitude of AC was kept at 5 mV, while the electrode was subjected to applied DC potentials of  $-0.5\text{ V}$  for EIS measurements in a frequency range of 100 kHz–10 mHz. A Luggin capillary was used to minimize errors due to  $iR$  drop of the electrolyte. The electrochemical performance of asymmetric supercapacitor assembled with two electrodes was investigated by cyclic voltammetry and chronopotentiometry techniques with  $\text{Li}_2\text{SO}_4$ /PVA gel as electrolyte and separator.

## 3. Results and Discussion

**3.1. Synthesis and Characterization.** XRD measurements are conducted on as-prepared film grown on partially exfoliated graphite. The XRD patterns of the film showed characteristic diffraction peaks of Hexagonal  $\text{WO}_3$  (JCPDS number 85-2460) in Figure 1(a). Hexagonal structure of  $\text{WO}_3$  has been reported to be attractive structures as an intercalation host for obtaining tungsten bronzes  $\text{M}_x\text{WO}_3$  ( $\text{M} = \text{H}^+$ ,  $\text{Li}^+$ ,  $\text{Na}^+$ , and  $\text{K}^+$ ) because of its special tunnel structure [10]. This tunnel structure may provide a smooth pathway for the movement of charges within  $\text{WO}_3$  electrode, giving rise to the charge storage capability for  $\text{WO}_3$  electrode

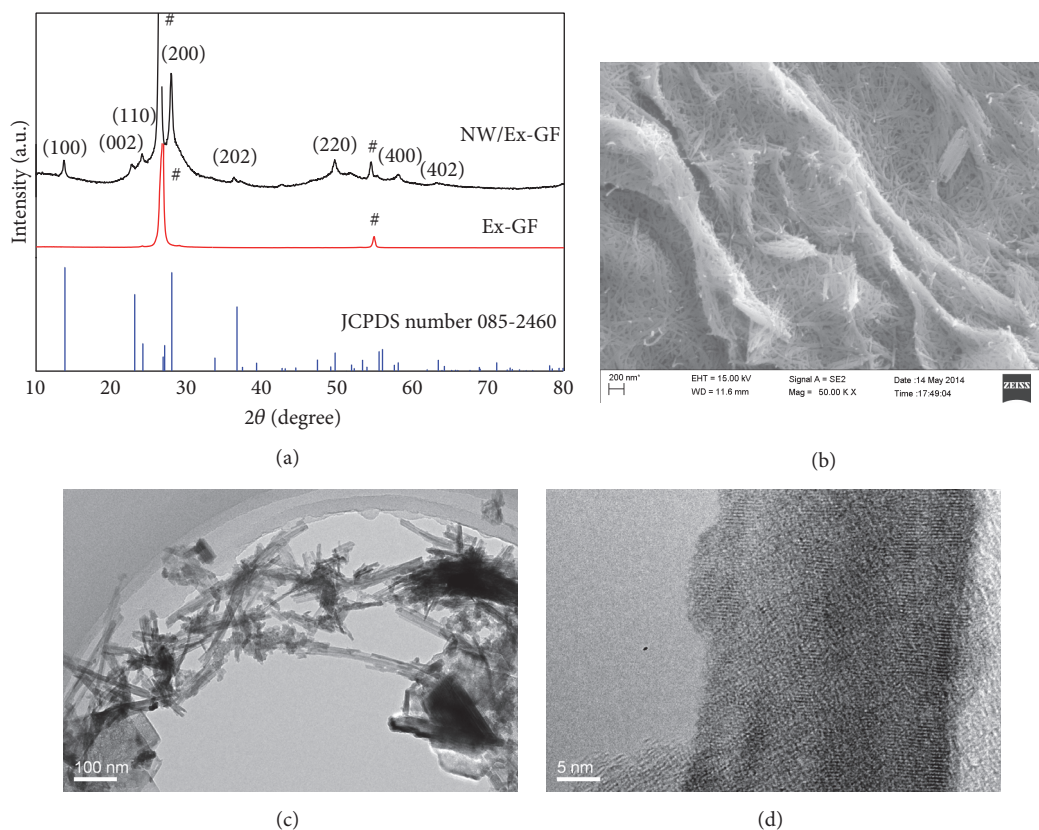


FIGURE 1: (a) XRD and (b) SEM image of ANW/Ex-GF and (c, d) TEM images of ANW/Ex-GF film. # refers to the characteristic diffraction peaks of the graphite or graphene partially exfoliated from the graphite.

material. On the other hand, crystalline  $\text{WO}_3$  is much more stable than amorphous  $\text{WO}_3$  due to the denser structure and lower dissolution rate in electrolytes, which is very important issue in terms of practical applications [28]. The sharp reflection peaks on XRD patterns indicate good crystallization and purity by seeded-induced hydrothermal reaction.

Surface morphologies of the films were investigated by SEM. As shown in Figure 1(b), uniform nanowires are clearly observed on the rough wrinkled electrode surface. These wrinkles are termed as thin graphene multilayers which are derived from electrochemically partial exfoliation [30]. From Figure 1(b), it can be seen that the exposed graphene edge planes stand on the surface with the thickness of several nanometers, which will provide more reactive surface centers and benefit electrochemical reactions. The average diameter of  $\text{WO}_3$  nanowires is about 10–20 nm and length is about 0.5–1  $\mu\text{m}$ , corresponding to the aspect ratios of ~50. The nanowires connect each other to form micropore and macropore structures. This one-dimensional porous structure with high specific area may provide more opportunity for the reactive centers on the film to contact with electrolyte and facilitate the charge transfer in the bulk of the film. The nanowires microstructure of  $\text{WO}_3$  is further investigated by TEM. Figure 1(c) shows  $\text{WO}_3$  nanowires randomly scattered on very thin transparent layers of graphene sheets with thickness about several nanometers. The high resolution of

TEM image in Figure 1(d) shows lattice fringes characteristic of crystalline materials.

XPS is employed to characterize the surface chemical compositions and valence state of samples. The XPS core level spectra of W 4f and survey spectrum of the sample surface are shown in Figure 2. In the spectrum of W 4f (Figure 2(a)), the peaks appearing at 35.7 and 37.9 eV can be assigned to W 4f<sub>7/2</sub> and W 4f<sub>5/2</sub> for W<sup>+6</sup> oxidation state. The survey spectrum of as-prepared nanowires  $\text{WO}_3$  reveals signals from W and O elements, indicating the composition of nanowire is  $\text{WO}_3$  species. Otherwise, a large amount of Na and Cl elements are clearly observed in  $\text{WO}_3$ , which comes from the precursor NaCl salt, suggesting that NaCl salt is more likely to be involved in  $\text{WO}_3$  crystal growth process. NaCl acts as capping agent and selectively absorbed onto the crystal planes parallel to the *c*-axes of  $\text{WO}_3$  crystal nucleus, resulting in the formation of uniform  $\text{WO}_3$  nanowires, which is similar to the growth mechanism of  $\text{WO}_3$  nanorods prepared by hydrothermal method without using seed-induced method [18]. It is worth noted that Na<sup>+</sup> and Cl<sup>-</sup> can be easily deintercalated from  $\text{WO}_3$  crystals during charge/discharge process in  $\text{Li}_2\text{SO}_4$  electrolyte as there is little Cl or Na element observed in the spectrum of  $\text{WO}_3$  after posttreatment (ANW) in Figure 2(b).

**3.2. Capacitive Performance of  $\text{WO}_3$  Nanowires on Graphene Sheets.** Figure 3(a) presents cyclic voltammograms of  $\text{WO}_3$

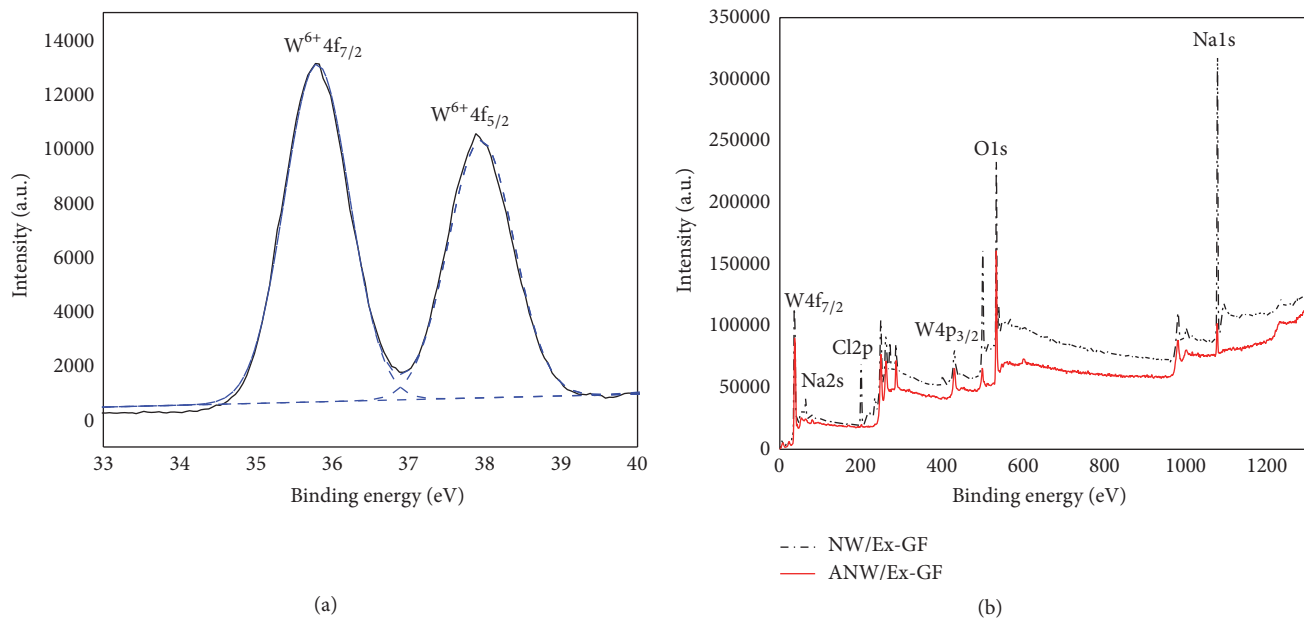


FIGURE 2: (a) High resolution XPS spectra of W 4f for NW/Ex-GF and (b) XPS survey spectra of ANW/Ex-GF and NW/Ex-GF.

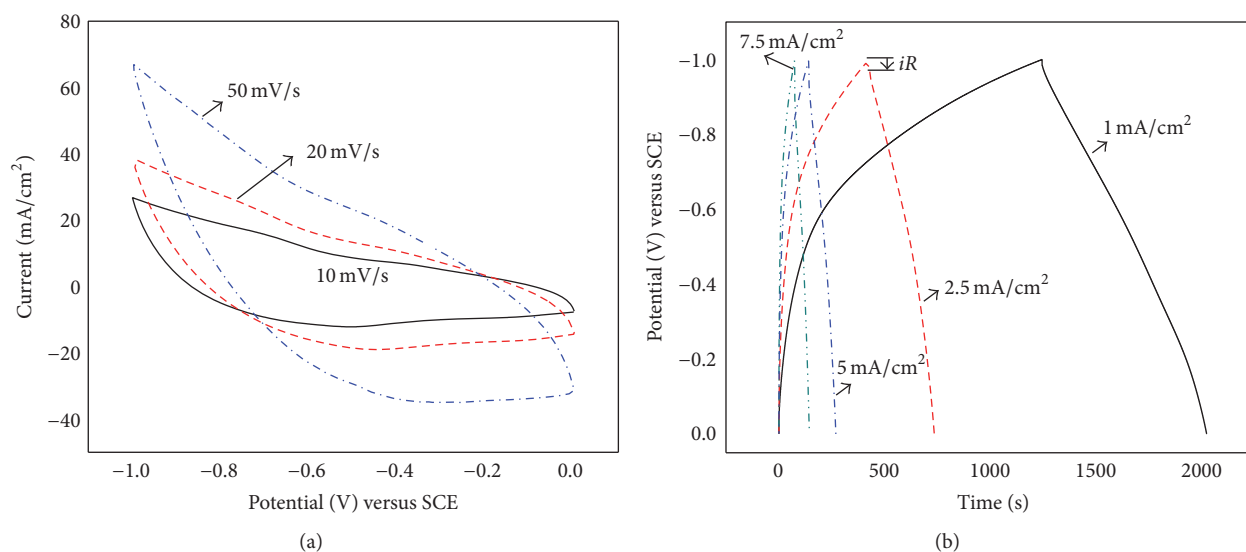


FIGURE 3: (a) CV profiles for ANW/Ex-GF at different scan rate. (b) Constant current charge/discharge profiles at different current densities for ANW/Ex-GF.

nanowires (ANW) with potential range from  $-1.0$  to  $0$  V in  $1$  M  $Li_2SO_4$  aqueous solution. The distorted rectangular shapes between  $10$  and  $50$   $mV s^{-1}$  reveal characteristic pseudocapacitive behavior based on the faradic redox reaction. The ANW film displayed electroactivity in the negative potential range because of  $Li^+$  and electrons insertion/extraction into/out of  $WO_3$  structures to form blue tungsten bronzes ( $Li_xWO_3$ ). The reduction and oxidation process can be represented by the following equation [27, 31]:



The apparent distortion at a higher scan rate is responsible for the electric polarization and irreversible reactions for  $WO_3$  crystals film.

Constant current charge/discharge experiments were conducted on ANW film by chronopotentiometry at various current densities, as shown in Figure 3(b). The charge/discharge curves show ideal linear profiles and nearly symmetric in negative potential range. This indicates that the as-obtained  $WO_3$  electrodes have good capacitive performance used as negative electrode. From the CV and CP profiles, the irreversibility and hysteresis phenomena are observed between anodic and cathodic scan profiles. It can be ascribed that the charge/discharge process is not completely

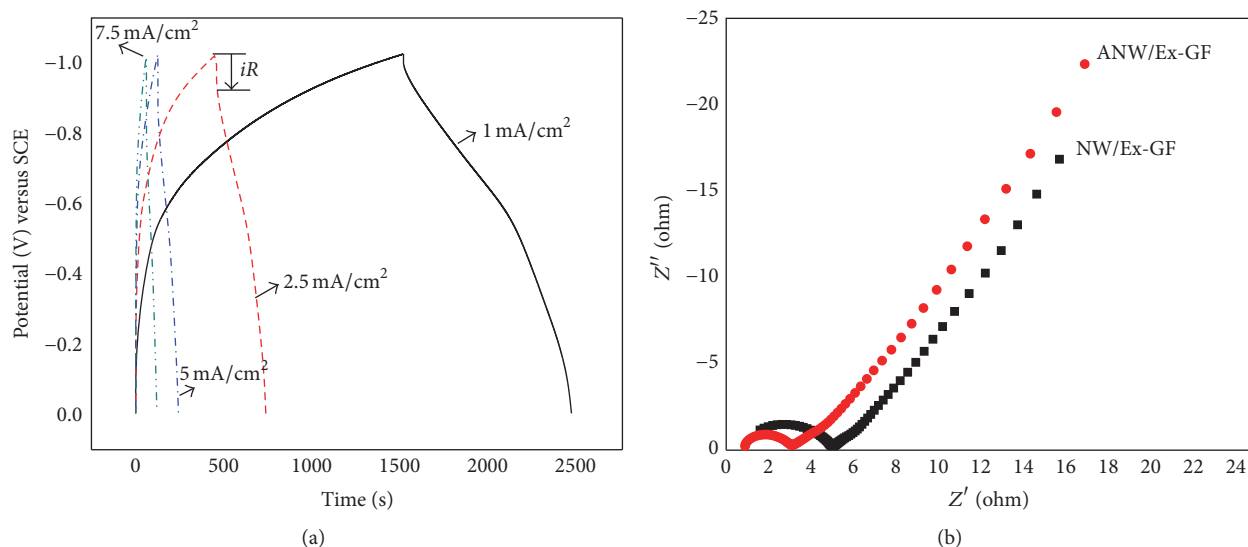


FIGURE 4: (a) Constant current charge/discharge profiles for NW/Ex-GF (b) Nyquist plots for ANW/Ex-GF and NW/Ex-GF electrodes measured at  $-0.5$  V DC potential in the frequency range of 100 kHz to 10 mHz.

reversible and the reduction form of tungsten bronzes of  $\text{Li}_x\text{WO}_3$  is not completely oxidized to  $\text{WO}_3$  during the anodic sweeps, leading to the coulombic efficiency ( $\eta$ ) lower than 1, which is 70%, 74%, 90%, and 98% at 1, 2.5, 5, and  $7.5 \text{ mA cm}^{-2}$ , respectively, calculated from (1):  $\eta = t_D/t_C \times 100$ , where  $t_D$  and  $t_C$  are discharging and charging times.

The area specific capacitance is calculated to be  $800 \text{ mF cm}^{-2}$  at a current density of  $1 \text{ mA cm}^{-2}$ , based on the equation:  $C_s = I \times \Delta t / (\Delta E \times S)$ , where  $C_s$  ( $\text{mF cm}^{-2}$ ) is the area specific capacitance,  $I$  and  $\Delta t$  are the charge/discharge current density and time, respectively,  $\Delta E$  is the potential window, and  $S$  is the projected area of the electrode. This remarkable area capacitance is comparable to those negative electrodes reported previously, such as  $\text{WO}_3/\text{PPy}$  ( $253 \text{ mF cm}^{-2}$ ) and PEDOT/SDS-GO composite ( $79.6 \text{ mF cm}^{-2}$ ) [26, 32]. The capacitance retained about 98.8%, 81.6% and 66.7% of its initial value at  $1 \text{ mA cm}^{-2}$  when charged/discharged at 2.5, 5, and  $7.5 \text{ mA cm}^{-2}$ , respectively, showing that the ANW electrode has good rate capability. For comparison, the galvanostatic charge/discharge profiles of  $\text{WO}_3$  electrode before treatment (NW) were also collected at various current densities. As shown in Figure 4(a), the CP profiles of NW electrode exhibit the same profiles, but larger  $iR$  drop than that of ANW electrode is observed, especially at a higher current density. The area specific capacitance of NW has the capacitance value of  $850 \text{ mF cm}^{-2}$ . But the capacitance retained about 73.4%, 61.0%, and 46.9% of its initial value at  $1 \text{ mA cm}^{-2}$  when charged/discharged at 2.5, 5, and  $7.5 \text{ mA cm}^{-2}$ , respectively. The larger  $iR$  and poorer rate capability of NW indicate the conductivity of the electrode can be improved by posttreatment. It seems reasonable that some  $\text{WO}_3$  on the electrode has been transformed irreversibly into higher conductivity of tungsten bronzes ( $\text{Li}_x\text{WO}_y$ ) after charge/discharge process in  $\text{Li}_2\text{SO}_4$  followed by annealing at  $\text{N}_2$  atmosphere.

Electrochemical impedance characteristics of the NW and ANW film were investigated at applied dc potentials

of  $-0.5$  V in  $1 \text{ M Li}_2\text{SO}_4$ . The Nyquist plots in the range of 100 kHz to 10 mHz are shown in Figure 4(b). There is a semicircle impedance arc in the high frequency region and a linear response in the low frequency region on the curve. This semicircle is attributed to the process at the electrode-electrolyte interface, which is expected to be the capacitance ( $C$ ) in parallel with the charge-transfer resistance ( $R_{ct}$ ) due to the charge exchange at the interface. A slope of steep line arising in the low frequency region on the curves accounts for a more faradic capacitive behavior of the electrode. The equivalent series resistance obtained from diameter of Nyquist plot for ANW is much smaller than that of NW, suggesting that the ANW has a lower resistance for the charge exchange, which is in agreement with CP results.

The stabilities of ANW and NW were also investigated by constant charge/discharge for 1000 cycles at current density of  $8 \text{ mA cm}^{-2}$  in  $1 \text{ M Li}_2\text{SO}_4$  solution in potential range between  $-1.0$  and  $0$  V. The specific capacitance can be retained about 78% for ANW after 1000 cycles, which is about 14% higher than NW, showing the better stability of ANW. The stability of NW electrode was improved by annealing at  $\text{N}_2$  atmosphere. It can be ascribed that the annealing process may reinforce the structure of  $\text{WO}_3$  nanowires and strengthen the combination between  $\text{WO}_3$  film and graphene sheets on the substrate.

**3.3. Comparison of Morphologies and Electrochemical Properties of  $\text{WO}_3$  Films Prepared by Different Process.** The morphologies of  $\text{WO}_3$  films prepared from different process were also studied. SEM image of  $\text{WO}_3$  film prepared with no graphene sheets is shown in Figure 5(a). It can be seen that  $\text{WO}_3$  nanowires grow on the relative smooth surface and most nanowires interconnect with each other to form circular structures, which result in a three-dimensional network with a highly open and porous structures, as shown in inset image of Figure 5(a). Interestingly, SEM image reveals that an individual nanowire is composed of many infinitesimal interconnected nanoparticles. These nanoparticles can provide

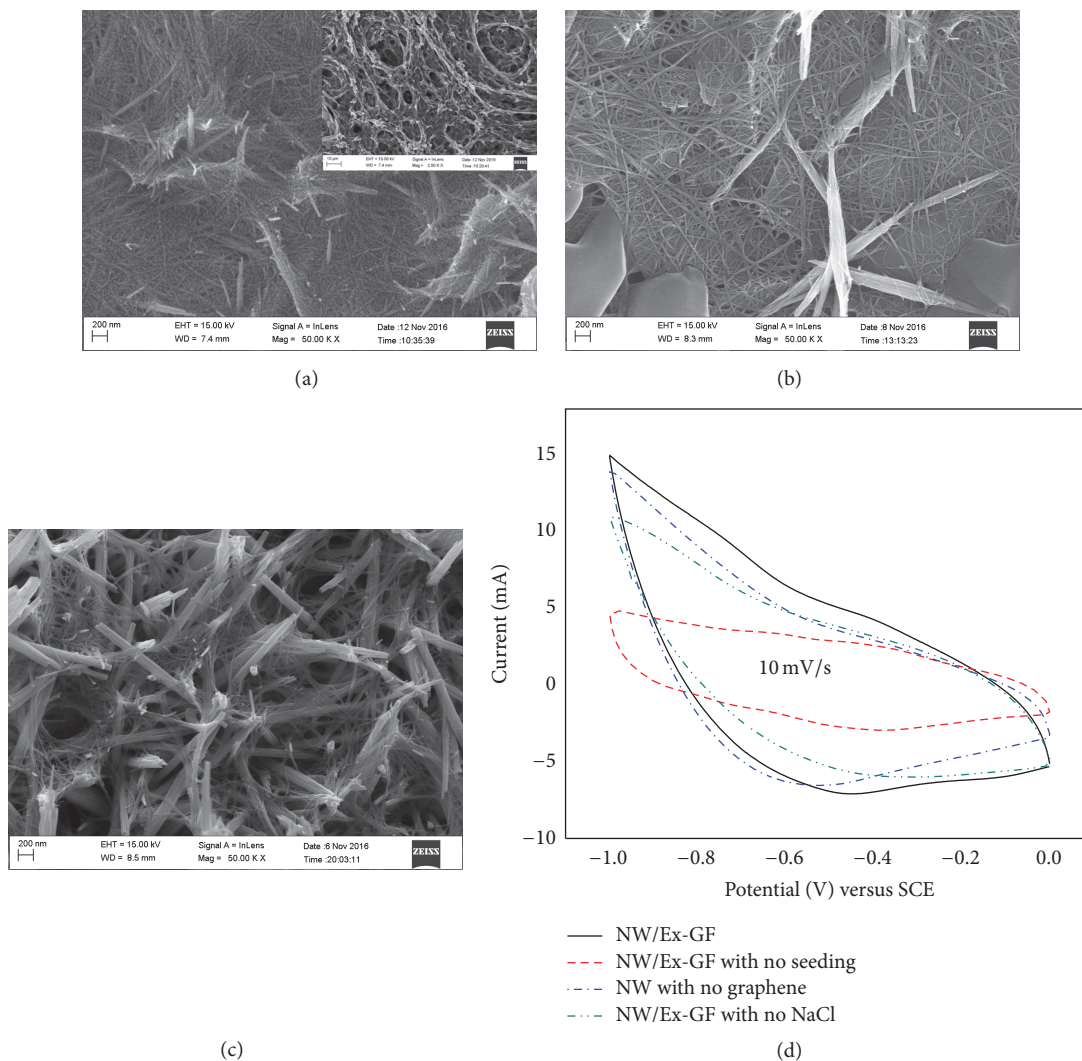


FIGURE 5: SEM images of WO<sub>3</sub> films prepared from different process: (a) with no graphene sheets on graphite foil; (b) with no WO<sub>3</sub> seeding; and (c) with no NaCl in the hydrothermal solution; (d) CVs of WO<sub>3</sub> electrodes prepared from different process.

high flexibility of nanowires and give rise to form circular structure of the film, which is very different from the crystallized nanowires grown on graphene sheets (Figure 1(b)). Figure 5(b) shows the morphology of the film prepared by hydrothermal process without using seed-induced method. Similar WO<sub>3</sub> crystalline nanowires can be seen on the surface, together with a large amount of big size of noncrystallized (or amorphous) phases, which indicates that pre-coating of nanosized WO<sub>3</sub> seeds on substrate is more beneficial to crystal nucleation and growth.

Figure 5(c) shows the morphology of WO<sub>3</sub> film prepared with no NaCl added in the deposition solution. It can be observed that the size of WO<sub>3</sub> nanowire is not uniform. Most of WO<sub>3</sub> nanowires appear to be aggregated into large dimension of bundles, which indicates that NaCl plays an important role in the formation of dispersive nanowires. It is considered reasonably that such metal ions as Li<sup>+</sup>, Na<sup>+</sup>, and K<sup>+</sup>, which can be intercalated into the crystal structures of tungsten oxide, may be selectively absorbed onto the facet

parallel to the *c*-axis of the hexagonal crystals, leading to preferential growth along the *c*-axis. Cl<sup>-</sup> ions can be absorbed on the surface as the counterpart simultaneously. Thus NaCl acts as capping agent and selectively absorbed onto the crystal planes, resulting in the formation of dispersive uniform WO<sub>3</sub> nanowires. Figure 5(d) shows the cyclic voltammograms of these films on graphite electrodes. The WO<sub>3</sub> nanowires on graphene sheets prepared by seed-induced method exhibits the highest current density among these electrodes, indicating that the preseeded nanosized WO<sub>3</sub>, graphene sheets on graphite, and NaCl capping agent are necessary for the formation of good crystallized WO<sub>3</sub> nanowires with a high specific surface area of the electrode.

**3.4. Capacitive Performance of PANI/MnO<sub>2</sub> Positive Electrode.** PANI/MnO<sub>2</sub> composite film on graphite (PM) was selected for the positive electrode to match the above ANW negative electrode for assembling asymmetric supercapacitor with Li<sub>2</sub>SO<sub>4</sub> as electrolyte. Figure 6(a) presents cyclic

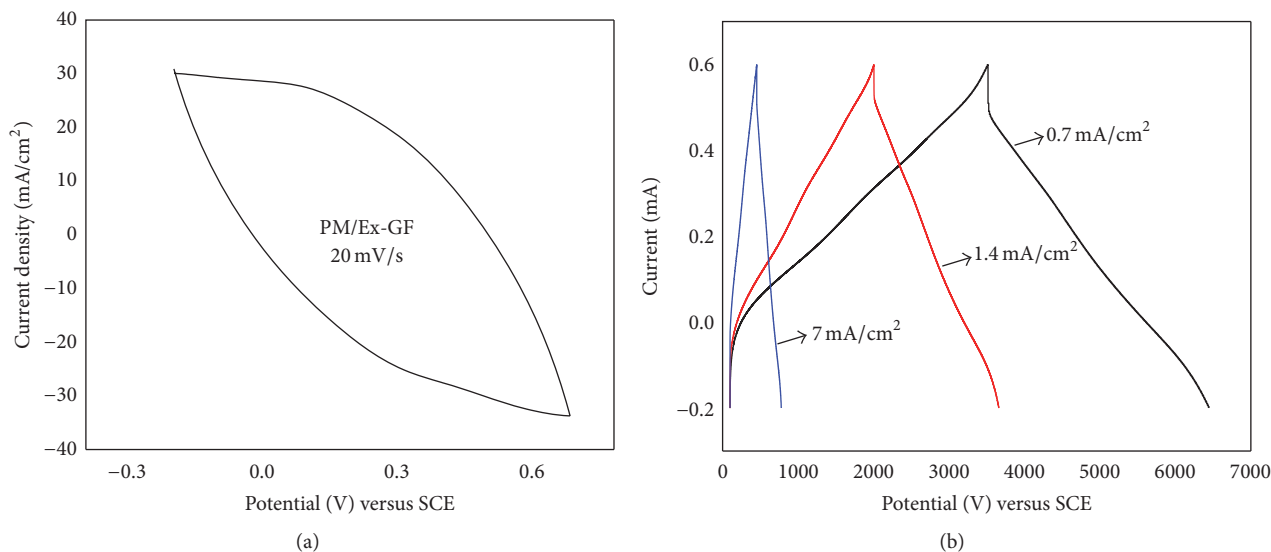


FIGURE 6: (a) CV curve of PM at scan rate of  $20 \text{ mV s}^{-1}$ ; (b) CP curves of PM at different current densities.

voltammogram of PM in  $1 \text{ M Li}_2\text{SO}_4$  aqueous electrolyte. PM composite electrode displays charge storage abilities in potential range from  $-0.2$  and  $0.6 \text{ V}$  at a high scan rate of  $20 \text{ mV s}^{-1}$ . The charge/discharge process on PANI/ $\text{MnO}_2$  composite electrode can be expressed as [33]

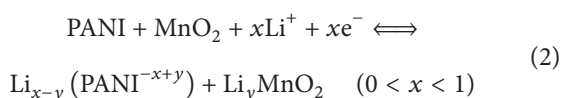


Figure 6(b) shows the CP profiles collected at different current densities. The CP curves show linear profiles and nearly symmetric in potential range from  $-0.2$  to  $0.6 \text{ V}$ , which is a typical pseudocapacitive behavior. The area specific capacitance of PM is calculated to be at  $1.16 \text{ F cm}^{-2}$ .

**3.5. Asymmetric Capacitor's Performance.** To evaluate the performance of ANW electrode in supercapacitors, an asymmetric supercapacitor was assembled by using PM and ANW as positive and negative electrodes, respectively, and with  $\text{Li}_2\text{SO}_4/\text{PVA}$  gel as the electrolyte as well as separator. From cyclic voltammograms of ANW and PM, the stable potential range for ANW is between  $-1.0$  and  $0 \text{ V}$ , and PM is between  $0$  and  $0.6 \text{ V}$ . Thus the cell voltage of asymmetric capacitor can be extended to  $1.6 \text{ V}$ , which originate from the sum of positive and negative potential range.

In order to obtain a stable  $1.6 \text{ V}$  operating potential window, it is necessary to balance the charges stored at the positive and negative electrodes. The stored charges ( $q$ ) are related to the specific capacitance ( $C_{sc}$ ), the potential window ( $\Delta V$ ), and the mass ( $m$ ) of the electrode according to  $q = C_{sc} \times \Delta V \times m$  [34]. On the basis of the specific capacitance values of the two materials and the potential windows, the mass ratio between PM and ANW of 1:2 was selected in the asymmetric supercapacitor cell. The fabricated asymmetric supercapacitor of PM//ANW shows a stable operating window up to  $1.6 \text{ V}$  in Figure 7(a). The typical

galvanostatic charge/discharge profiles of the supercapacitor between  $0.0$  and  $1.6 \text{ V}$  at different current densities are shown in Figure 7(b). The charge/discharge curves are nearly symmetric linear, indicating a typical pseudocapacitive behavior of supercapacitor. The specific capacitance of the PM//ANW capacitor is calculated to be  $2.5 \text{ F cm}^{-3}$  at a current density of  $1 \text{ mA cm}^{-2}$  (the total volume of the cell is about  $0.1 \text{ cm}^3$ ). It is about 94.7%, 80%, and 64% of its initial value at  $1 \text{ mA cm}^{-2}$  when charged/discharged at 2, 5 and  $10 \text{ mA cm}^{-2}$ , respectively, showing that the capacitor has good rate capability. The energy density  $E_s$  of the asymmetric capacitor is found to be  $0.88 \text{ mWh cm}^{-3}$  at power density of  $9.16 \text{ mW cm}^{-3}$ , calculated by the equation  $E_s = (1/2)C_s V^2$ , where  $C_s$  is the area specific capacitance of electrodes and  $V$  is the operating voltage of the cell [34].

## 4. Conclusion

$\text{WO}_3$  nanowires grown on graphene sheets partially exfoliated from graphite foil exhibited good pseudocapacitive performance in the negative potential window of  $-1.0$  to  $0 \text{ V}$  versus SCE in  $1 \text{ M Li}_2\text{SO}_4$  aqueous solution. It was found that precoating of nanosized  $\text{WO}_3$  seeds and graphene sheets on substrate is more beneficial to crystal nucleation and growth, resulting in the formation of uniform crystallized  $\text{WO}_3$  nanowires on substrate. The asymmetric capacitor assembled with  $\text{WO}_3$  nanowires and PANI/ $\text{MnO}_2$  composite as negative and positive electrodes can be operated over a large cell voltage of  $1.6 \text{ V}$  and displays a high energy density of  $0.88 \text{ mWh cm}^{-3}$  at power density of  $9.16 \text{ mW cm}^{-3}$ . With these properties,  $\text{WO}_3$  nanowires on graphene sheets can be a promising negative electrode material for asymmetry capacitors.

## Competing Interests

The authors declare that they have no competing interests.

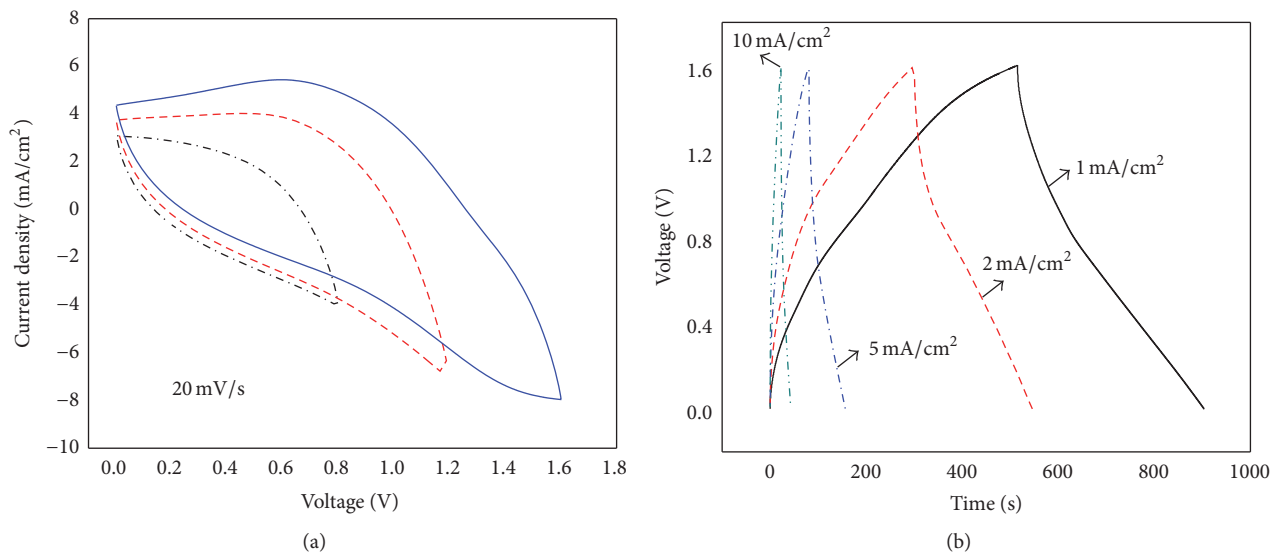


FIGURE 7: (a) CV curves of supercapacitor assembled with ANW/Ex-GF as negative electrode and PM/Ex-GF as positive electrode; (b) CP curves of supercapacitor at different current densities.

## Acknowledgments

The authors acknowledge Liaoning Key Laboratory of Functional Textile Materials and Dalian Institute of Chemical Physics for the technical support of SEM, XRD, TEM, and BET measurements. The authors acknowledge financial support by National Natural Science Foundation of China (Project no. 51343002) and Liaoning Province new Ph.D. start-up fund (Project no. 20131039).

## References

- [1] D. Meng, N. M. Shaalan, T. Yamazaki, and T. Kikuta, "Preparation of tungsten oxide nanowires and their application to NO<sub>2</sub> sensing," *Sensors and Actuators, B: Chemical*, vol. 169, pp. 113–120, 2012.
- [2] F. Han, H. Li, L. Fu, J. Yang, and Z. Liu, "Synthesis of S-doped WO<sub>3</sub> nanowires with enhanced photocatalytic performance towards dye degradation," *Chemical Physics Letters*, vol. 651, pp. 183–187, 2016.
- [3] C. Guo, S. Yin, M. Yan, M. Kobayashi, M. Kakihana, and T. Sato, "Morphology-controlled synthesis of W<sub>18</sub>O<sub>49</sub> nanostructures and their near-infrared absorption properties," *Inorganic Chemistry*, vol. 51, no. 8, pp. 4763–4771, 2012.
- [4] G. Li, S. Zhang, C. Guo, and S. Liu, "Absorption and electrochromic modulation of near-infrared light: realized by tungsten suboxide," *Nanoscale*, vol. 8, no. 18, pp. 9861–9868, 2016.
- [5] M. Yan, G. Li, C. Guo et al., "WO<sub>3-x</sub> sensitized TiO<sub>2</sub> spheres with full-spectrum-driven photocatalytic activities from UV to near infrared," *Nanoscale*, vol. 8, no. 41, pp. 17828–17835, 2016.
- [6] Z.-X. Cai, H.-Y. Li, X.-N. Yang, and X. Guo, "NO sensing by single crystalline WO<sub>3</sub> nanowires," *Sensors and Actuators, B: Chemical*, vol. 219, pp. 346–353, 2015.
- [7] S. Shendage, V. Patil, S. Vanalakar et al., "Sensitive and selective NO<sub>2</sub> gas sensor based on WO<sub>3</sub> nanoplates," *Sensors and Actuators B: Chemical*, vol. 240, pp. 426–433, 2017.
- [8] N. V. Hieu, V. V. Quang, N. D. Hoa, and D. Kim, "Preparing large-scale WO<sub>3</sub> nanowire-like structure for high sensitivity NH<sub>3</sub> gas sensor through a simple route," *Current Applied Physics*, vol. 11, no. 3, pp. 657–661, 2011.
- [9] M. Govender, L. Shikwambana, B. W. Mwakikunga, E. Sideras-Haddad, R. M. Erasmus, and A. Forbes, "Esopen accessformation of tungsten oxide nanostructures by laser pyrolysis: stars, fibres and spheres," *Nanoscale Research Letters*, vol. 6, no. 1, article no. 166, 2011.
- [10] A. Phuruangrat, D. J. Ham, S. J. Hong, S. Thongtem, and J. S. Lee, "Synthesis of hexagonal WO<sub>3</sub> nanowires by microwave-assisted hydrothermal method and their electrocatalytic activities for hydrogen evolution reaction," *Journal of Materials Chemistry*, vol. 20, no. 9, pp. 1683–1690, 2010.
- [11] C. Guo, S. Yin, Y. Huang, Q. Dong, and T. Sato, "Synthesis of W<sub>18</sub>O<sub>49</sub> nanorod via ammonium tungsten oxide and its interesting optical properties," *Langmuir*, vol. 27, no. 19, pp. 12172–12178, 2011.
- [12] V. Chakrapani, J. Thangala, and M. K. Sunkara, "WO<sub>3</sub> and W<sub>2</sub>N nanowire arrays for photoelectrochemical hydrogen production," *International Journal of Hydrogen Energy*, vol. 34, no. 22, pp. 9050–9059, 2009.
- [13] B. Chai, J. Li, Q. Xu, and K. Dai, "Facile synthesis of reduced graphene oxide/WO<sub>3</sub> nanoplates composites with enhanced photocatalytic activity," *Materials Letters*, vol. 120, pp. 177–181, 2014.
- [14] R. Ganesan, I. Perelshtein, and A. Gedanken, "Biotemplated synthesis of single-crystalline W<sub>18</sub>O<sub>49</sub>@C core-shell nanorod and its capacitance properties," *Journal of Physical Chemistry C*, vol. 112, no. 6, pp. 1913–1919, 2008.
- [15] Y. Shingaya, T. Nakayama, and M. Aono, "Epitaxial growth of WO<sub>x</sub> nanorod array on W(001)," *Science and Technology of Advanced Materials*, vol. 5, no. 5-6, pp. 647–649, 2004.
- [16] P. M. Rao and X. Zheng, "Flame synthesis of tungsten oxide nanostructures on diverse substrates," *Proceedings of the Combustion Institute*, vol. 33, no. 2, pp. 1891–1898, 2011.
- [17] J. Polleux, A. Gurlo, N. Barsan, U. Weimar, M. Antonietti, and M. Niederberger, "Template-free synthesis and assembly

- of single-crystalline tungsten oxide nanowires and their gas-sensing properties,” *Angewandte Chemie*, vol. 118, pp. 267–271, 2006.
- [18] J. Wang, E. Khoo, P. S. Lee, and J. Ma, “Synthesis, assembly, and electrochromic properties of uniform crystalline  $\text{WO}_3$  nanorods,” *Journal of Physical Chemistry C*, vol. 112, no. 37, pp. 14306–14312, 2008.
- [19] H. Wei, X. Yan, S. Wu, Z. Luo, S. Wei, and Z. Guo, “Electropolymerized polyaniline stabilized tungsten oxide nanocomposite films: electrochromic behavior and electrochemical energy storage,” *Journal of Physical Chemistry C*, vol. 116, no. 47, pp. 25052–25064, 2012.
- [20] C. Jo, I. Hwang, J. Lee, C. W. Lee, and S. Yoon, “Investigation of pseudocapacitive charge-storage behavior in highly conductive ordered mesoporous tungsten oxide electrodes,” *Journal of Physical Chemistry C*, vol. 115, no. 23, pp. 11880–11886, 2011.
- [21] X. Li, Z. Wang, Y. Qiu, Q. Pan, and P. Hu, “3D graphene/ZnO nanorods composite networks as supercapacitor electrodes,” *Journal of Alloys and Compounds*, vol. 620, pp. 31–37, 2015.
- [22] L. Gao, X. Wang, Z. Xie et al., “High-performance energy-storage devices based on  $\text{WO}_3$  nanowire arrays/carbon cloth integrated electrodes,” *Journal of Materials Chemistry A*, vol. 1, no. 24, pp. 7167–7173, 2013.
- [23] H. Peng, G. Ma, K. Sun, J. Mu, M. Luo, and Z. Lei, “High-performance aqueous asymmetric supercapacitor based on carbon nanofibers network and tungsten trioxide nanorod bundles electrodes,” *Electrochimica Acta*, vol. 147, pp. 54–61, 2014.
- [24] Y. Tian, S. Cong, W. Su et al., “Synergy of  $\text{W18O49}$  and polyaniline for smart supercapacitor electrode integrated with energy level indicating functionality,” *Nano Letters*, vol. 14, no. 4, pp. 2150–2156, 2014.
- [25] L. Ma, X. Zhou, L. Xu et al., “Hydrothermal preparation and supercapacitive performance of flower-like  $\text{WO}_3 \cdot \text{H}_2\text{O}$ /reduced graphene oxide composite,” *Colloids and Surfaces A: Physicochemical and Engineering Aspects*, vol. 481, pp. 609–615, 2015.
- [26] F. Wang, X. Zhan, Z. Cheng et al., “Tungsten oxide@polypyrrole core-shell nanowire arrays as novel negative electrodes for asymmetric supercapacitors,” *Small*, vol. 11, no. 6, pp. 749–755, 2015.
- [27] B.-X. Zou, Y. Liang, X.-X. Liu, D. Diamond, and K.-T. Lau, “Electrodeposition and pseudocapacitive properties of tungsten oxide/polyaniline composite,” *Journal of Power Sources*, vol. 196, no. 10, pp. 4842–4848, 2011.
- [28] B.-X. Zou, Y. Gao, B. Liu, Y. Yu, and Y. Lu, “Three dimensional heteroatom-doped carbon composite film for flexible solid-state supercapacitors,” *RSC Advances*, vol. 6, no. 6, pp. 4483–4489, 2016.
- [29] B. Reichman and A. J. Bard, “The electrochromic process at  $\text{WO}_3$  electrodes prepared by vacuum evaporation and anodic oxidation of W,” *Journal of the Electrochemical Society*, vol. 126, no. 4, pp. 583–591, 1979.
- [30] Y. Song, J.-L. Xu, and X.-X. Liu, “Electrochemical anchoring of dual doping polypyrrole on graphene sheets partially exfoliated from graphite foil for high-performance supercapacitor electrode,” *Journal of Power Sources*, vol. 249, pp. 48–58, 2014.
- [31] X. Cui, H. Zhang, X. Dong et al., “Electrochemical catalytic activity for the hydrogen oxidation of mesoporous  $\text{WO}_3$  and  $\text{WO}_3/\text{C}$  composites,” *Journal of Materials Chemistry*, vol. 18, no. 30, pp. 3575–3580, 2008.
- [32] H. Zhou, G. Han, D. Fu, Y. Chang, Y. Xiao, and H.-J. Zhai, “Petal-shaped poly(3,4-ethylenedioxythiophene)/sodium dodecyl sulfate-graphene oxide intercalation composites for high-performance electrochemical energy storage,” *Journal of Power Sources*, vol. 272, pp. 203–210, 2014.
- [33] Q. Cheng, J. Tang, J. Ma, H. Zhang, N. Shinya, and L.-C. Qin, “Graphene and nanostructured  $\text{MnO}_2$  composite electrodes for supercapacitors,” *Carbon*, vol. 49, no. 9, pp. 2917–2925, 2011.
- [34] H. Gao, F. Xiao, C. B. Ching, and H. Duan, “High-performance asymmetric supercapacitor based on graphene hydrogel and nanostructured  $\text{MnO}_2$ ,” *ACS Applied Materials and Interfaces*, vol. 4, no. 5, pp. 2801–2810, 2012.



**Hindawi**

Submit your manuscripts at  
<https://www.hindawi.com>

